

Proton spectra from ultraintense laser–plasma interaction with thin foils: Experiments, theory, and simulation

M. Allen,^{1–3, a)} Y. Sentoku,² P. Audebert,⁴ A. Blazevic,⁵ T. Cowan,^{2,3} J. Fuchs,⁴ J. C. Gauthier,⁴ M. Geissel,⁵ M. Hegelich,⁶ S. Karsch,⁶ E. Morse,¹ P. K. Patel,³ and M. Roth⁵

¹Department of Nuclear Engineering, University of California, Berkeley, Berkeley, California 94720

²General Atomics, P.O. Box 85608, San Diego, California 92186

³Lawrence Livermore National Laboratory, Livermore, California 94550

⁴Laboratoire pour l'Utilisation des Lasers Intenses, Ecole Polytechnique, 91128 Palaiseau, France

⁵Technische Universität Darmstadt, 64289 Darmstadt, Germany

⁶Max-Planck-Institut für Quantenoptik, 85748 Garching, Germany

(Received 14 April 2003; accepted 22 May 2003)

A beam of high energy ions and protons is observed from targets irradiated with intensities up to 5×10^{19} W/cm². Maximum proton energy is shown to strongly correlate with laser-irradiance on target. Energy spectra from a magnetic spectrometer show a plateau region near the maximum energy cutoff and modulations in the spectrum at approximately 65% of the cutoff energy. Presented two-dimensional particle-in-cell simulations suggest that modulations in the proton spectrum are caused by the presence of multiple heavy-ion species in the expanding plasma. © 2003 American Institute of Physics. [DOI: 10.1063/1.1592154]

I. INTRODUCTION

Charged particles accelerated up to energies of several MeV have been observed from laser–plasma interactions for more than 20 years. Early experiments with long pulse (several nanoseconds) lasers incident on thin foils and wires at the Los Alamos National Laboratory Helios facility observed protons and multiple charge states of carbon accelerated up to velocities of 10^9 cm/s (corresponding to energies up to ~ 0.5 MeV).¹ It was shown that these protons and carbon ions are present regardless of target material due to hydrocarbon contaminants inside the vacuum system.² The acceleration mechanism was shown to be the result of an electrostatic field due to charge separation in the underdense region of the expanding plasma. The maximum ion acceleration correlated strongly with hot electron temperature.

In the past several years, the rapid development of short-pulse, ultraintense lasers³ opened the door to the new field of relativistic laser–plasma interactions. Recent experiments^{4,5,8–13} with foil targets showing the acceleration of protons up to energies of 58 MeV, and heavier charged particles up to hundreds of MeV. Various mechanisms have been proposed to explain the observed results, such as ponderomotive acceleration from the front surface of the target,^{4,5} electrostatic sheath acceleration from the back surface of the target^{8,9,10} or a combination of the two.⁶

When laser intensities begin to exceed $\sim 10^{18}$ W/cm², electron oscillations in the laser electric field become relativistic. In this regime, various linear and nonlinear laser–plasma processes (such as vacuum heating, self-focusing, $J \times B$ forces) can generate electron temperatures in the MeV

range and drive electrons through the solid density region of the target.⁷

In the model presented by Hatchett *et al.*,⁸ of the electrons that penetrate the back surface of the target, only a few can actually escape. The rest are pulled back by the positive potential the target has acquired and oscillate through the target while drifting transversely. At a snapshot in time, this hot electron cloud resembles a sheath on the rear surface of the target. The resultant electric field due to this sheath is strong enough to field ionize and accelerate ions from the rear surface into vacuum. This mechanism, now referred to as Target Normal Sheath Acceleration (TNSA), is described in greater detail by Refs. 8 and 9. It is beneficial to restate Hatchett's and Wilk's explanation that this model differs from the early long-pulse mechanism in that the laser pulse is so short, that the electrostatic sheath is created by the hot electrons while the rear surface of the target is still cold. This allows for a strong charge separation over a small scale length, which produces a strong electric field given by

$$|\mathbf{E}| \approx \frac{kT_{\text{hot}}}{e\lambda_D}, \quad (1)$$

where $\lambda_D = (\epsilon_0 kT_{\text{hot}}/e^2 n_e)^{1/2}$ is the standard electron Debye length. Typical hot electron temperatures and densities of $kT_{\text{hot}} \sim 2$ MeV and $n_e \sim 10^{19}$ cm⁻³ lead to a Debye length of $\lambda_D \sim 3$ μm and an electric field $E > 10^{12}$ V/m. If contaminants are present on the rear surface, they will be field ionized and accelerated normal to the surface of the target. The electric field will continue to accelerate ions until the electrons have sufficiently cooled (by adiabatic cooling or by accelerating ions) such that the Debye length becomes equal to the ion scale length, $\lambda_D = \lambda_{\text{ion}} = c_s t$, where c_s is the ion sound speed and t is time. At this point, the hot-electron Debye length is equal to the local ion scale length, and a

^{a)}Electronic mail: mallen@nuc.berkeley.edu

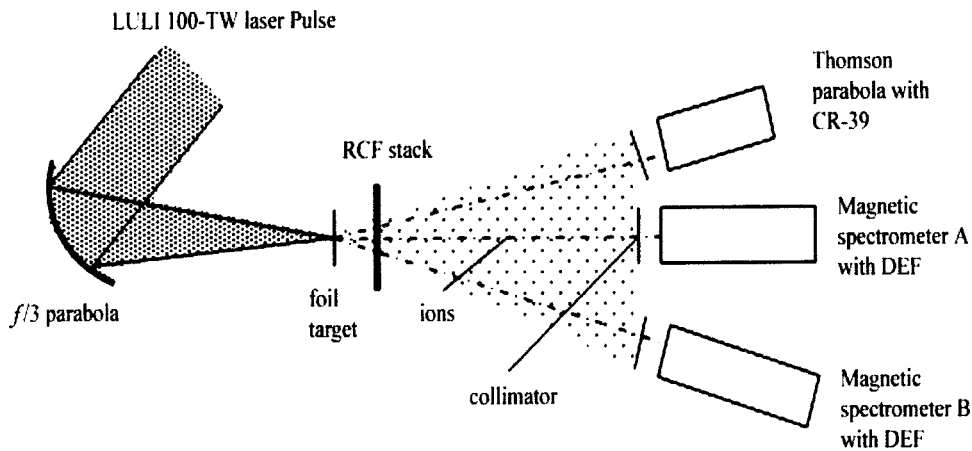


FIG. 1. Experimental setup showing RCF stack, magnetic spectrometers, and Thomson parabolas used to detect ions from rear surface of laser-target.

strong charge separation no longer exists; the charged particles drift at the velocity they have acquired.

In this paper, we report on electron and proton spectra observed from the interaction of an ultraintense laser pulse with thin foils. Section II describes the experimental setup and the diagnostics used to detect charged particles. Experimental results such as electron and proton spectra, are presented in Sec. III. In Sec. IV, we discuss the data, and present a 2D simulation that agrees well with the experimental results.

II. EXPERIMENTAL SETUP

The experiments were performed at the 100 TW laser facility of the Laboratoire pour l'Utilisation des Lasers Intenses (LULI). The laser system is capable of delivering pulses of 30 J in 300 fs at a wavelength of $\lambda = 1.058 \mu\text{m}$. The pulses were focused onto thin foils at normal incidence by an $f/3$ off-axis parabola with a $1/e^2$ focal spot size radius of $8 \mu\text{m}$, producing an intensity on target of up to $5 \times 10^{19} \text{ W/cm}^2$. A pedestal of amplified spontaneous emission (ASE) was present from 2 ns before the main pulse at a level of 10^{-7} of the main pulse intensity. Laser targets for the experiments presented here were either Au or Al foils of thickness varying from $10 \mu\text{m}$ up to $48 \mu\text{m}$. On occasion an additional layer of CH (tens of Å thick) was added to the back of the foil target to seed proton yield.

The experimental setup shown in Fig. 1 shows the orientation of the three primary diagnostics used for ion detection. A stack of radiochromic film is placed 5–7 cm behind the target to record the angular distribution of the emitted proton beam.¹¹ Radiochromic film (RCF) is a dosimetry film that measures radiation dose, in this case from the proton energy deposition. The RCF stack is protected from target debris by a $13 \mu\text{m}$ thick Al foil, while a slit in the RCF stack provides an unobstructed line of sight to the target from the proton spectrometers and Thomson parabolas. The magnetic spectrometers described in Ref. 12 can be mounted in either 0° (spectrometer A) or 13° (spectrometer B) to the normal of the target rear surface, at a distance of approximately 1 m from the target. Permanent 5 kG magnets disperse charged particles (protons or electrons) according to their momentum on to KODAK Direct Exposure Film (DEF) wrapped in pho-

tographic paper that blocks visible light. Using nuclear emulsion track detectors in conjunction with the film showed that the response function of electrons in DEF is linear with intensity over the range of observation.¹² Recommendations when using DEF to diagnosis protons are discussed in Sec. III. The minimum detection threshold of the magnetic spectrometers is 3 MeV for protons and 0.2 MeV for electrons.

A $1.8 \text{ mm} \times 5.0 \text{ mm}$ collimator in the spectrometers was used to achieve high resolution in the direction of dispersion. At a distance of 1 m from target chamber center, this gave a solid angle of $\sim 9 \times 10^{-6}$ sr. Spectra from the magnetic spectrometers were deconvolved from the rectangular aperture function by the nonlinear method described by Jansson in Ref. 14.

Spectra of various charge states of ions heavier than protons were obtained by Thomson parabolas using a nuclear track detector, CR-39, to record the ions.¹³

III. EXPERIMENTAL RESULTS

Figure 2 shows a scan of the DEF and corresponding electron spectrum from spectrometer A. This particular laser-shot was of 24.6 J on a target of $20 \mu\text{m}$ Au with 50 \AA CH on the back surface. Analytically, the hot-electron temperature can be estimated by the ponderomotive potential of the laser-pulse, $kT_H \sim U_p \sim 1 \text{ MeV} \times (I\lambda^2/10^{19} \text{ W/cm}^2 \mu\text{m}^2)$ in the relativistic regime. With respect to LULI laser parameters, this gives $kT_H \sim 2.6 \text{ MeV}$. Fitting a Boltzman distribution, $N(E_e) \sim \exp(-E_e/kT_H)$, to our measured electron spectrum gives a best fit $kT_H \sim 2.1 \text{ MeV}$ in good agreement with the predicted value.

The proton film data and corresponding spectra shown in Fig. 3 are typical and highly repeatable results for a medium energy laser shot (22.2 J) on a metallic target of $\sim 50 \mu\text{m}$ thickness. Modulations in the density distribution are visible as lines in the images of the data in the inset.

The maximum cutoff energy decreases at angles greater than normal incidence. At 13° , the maximum energy was approximately 70% of the cutoff energy observed from protons at normal incidence. Figure 4 plots the proton cutoff energy in spectrometer B relative to spectrometer A against the laser energy for different laser shots. Over the range of

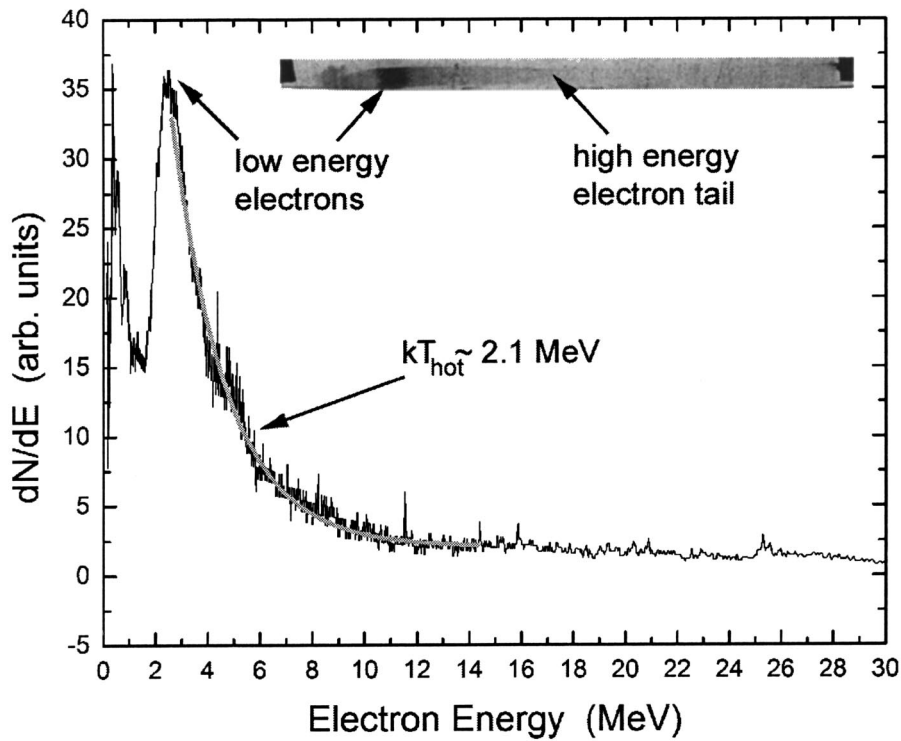


FIG. 2. LULI shot #6261751a. Electron film from magnetic spectrometer. An experimental fit of $kT_{hot} \sim 2.1$ MeV agrees well with theoretically predicted electron temperature.

20–30 J of laser energy, the ratio of the maximum cutoff energies is approximately constant.

Figure 5 plots the dependence of ion energy against $I\lambda^2$ ($\text{W cm}^{-2} \mu\text{m}^2$), including only data from the spectrometer at 0° . The observed correlation between ion energy and $I\lambda^2$ is consistent with recent experiments involving short pulse

lasers¹⁵ and earlier experiments from high irradiance, nanosecond, $10.6 \mu\text{m}$ laser plasma interactions.² Clark *et al.* report a scaling of $E_{max} \propto (I\lambda^2)^{0.4}$ up to irradiances of $10^{18} \text{ W cm}^{-2} \mu\text{m}^2$ and a scaling of $E_{max} \propto (I\lambda^2)^{0.5}$ beyond $10^{18} \text{ W cm}^{-2} \mu\text{m}^2$ when the oscillation velocity of the fast electrons becomes relativistic.¹⁵ The best least squares fit for

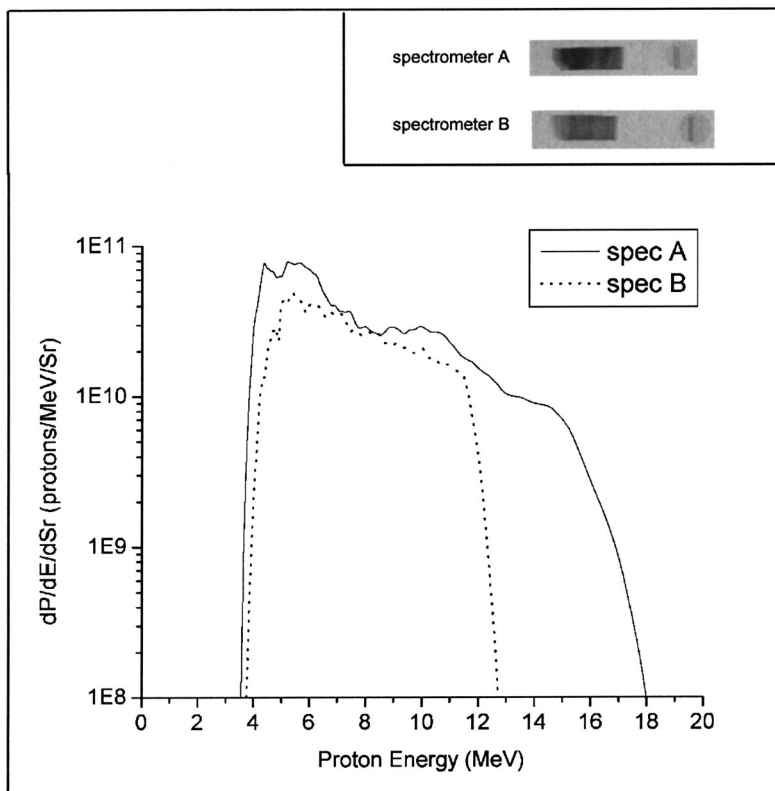


FIG. 3. Proton spectra from LULI shot #06261651. Laser energy was 22.2 J, and laser-target was $48 \mu\text{m Au} + 20 \text{ \AA CH}$. Proton film is shown in the figure inset. Spectrometer A and spectrometer B are at 0° and 13° , respectively to the back of the target.

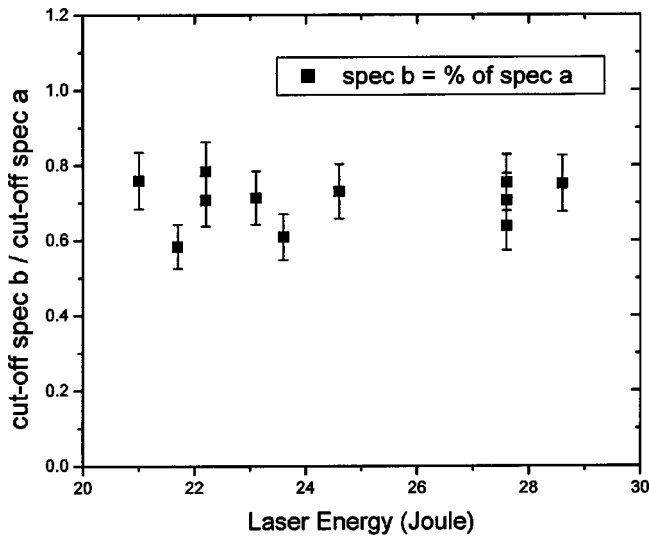


FIG. 4. Ratio of maximum proton energy at zero degrees to that achieved at 13°.

our data was $E_{\max} \propto (I\lambda^2)^{0.5}$, which gave a chi-squared per degree of 0.44. This is consistent with results previously reported.

The proton spectra presented in Fig. 3 show modulations in the distribution. These modulations are more clearly seen on a linear scale as shown in Fig. 6. The spectrum presented in Fig. 6 shows three distinct areas of interest: a plateau near the high energy cutoff, a peak near 9 MeV (labeled A) and another peak near 5 MeV (labeled B).

The plateau that appears near the high energy cutoff in the spectrum is sometimes sharply peaked, and believed to be an indication of an initial scale length density profile on the back surface. The protons that exist between the negatively charged Debye sheath and the positively charged internal ion-sheet, will have the same acceleration and contribute to bunching at the high energy cutoff.⁸

The peak labeled A in Fig. 6 appears on the data in the range 7–10 MeV. Of the 54 proton spectra recorded during

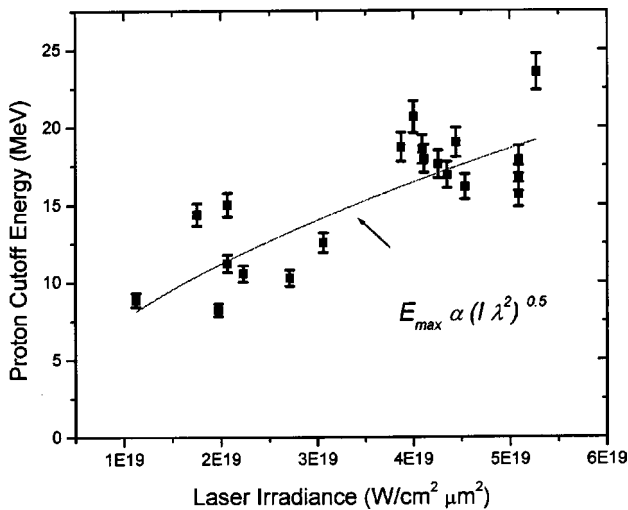


FIG. 5. Fit of maximum proton energy as a function of $I\lambda^2$ to a power law gives a dependence of $E_{\max} \propto (I\lambda^2)^{0.5}$.

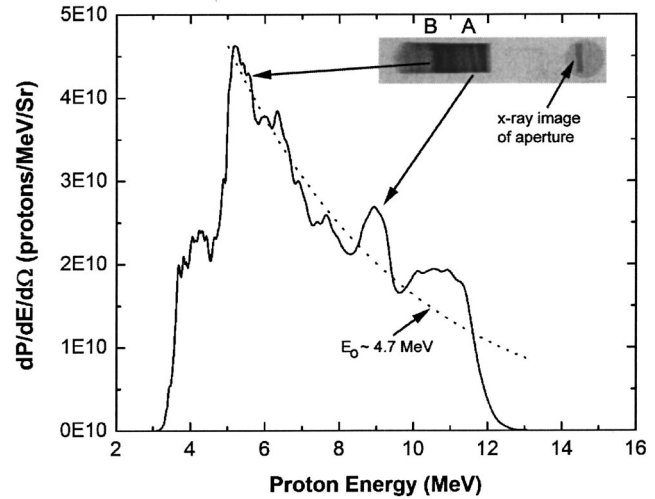


FIG. 6. Proton film data and spectrum of LULI shot #06282048. Laser energy was 21.1 J, and laser-target was a 48 μm Au foil. Two distinct lines are visible in the spectrum. Line A is thought to be due to the presence of carbon ions. Line B is due to protons reaching their Bragg peak in the second emulsion layer of DEF.

the experiment, 17 (approximately 30%) have distinguishable modulations similar to that shown in the figure. Modulations in this region of the proton spectrum have not been observed previously at this energy, and are thought to be the effect of heavier ions also accelerated from the back surface of the target. The heavier ions, in this case, are various charge states of carbon which are present on the target on the form of hydrocarbon contaminants.

The Thomson parabola recorded the acceleration of heavier ions from targets with typical levels of hydrocarbon contamination and those that had been heated to remove protons.¹³ Table I shows the yield of each ion species in the case of a heated and unheated target aluminum. The values listed for the unheated target are used as the relative concentrations of the carbon ions for the PIC code developed to model this effect, which is described more extensively in Sec. IV.

The spectral line marked B in Fig. 6 (the strong line at 5 MeV), is due to ranging out of protons in the second layer of DEF. The peak arises because the film has a thin emulsion layer of approximately 13 μm on both sides of a plastic substrate that is approximately 185 μm thick. Using the chemical composition of DEF,¹⁶ and adding the chemical composition of the paper used to protect the film from light leaks, TRIM calculations showed that protons reach their Bragg peak in the back layer of emulsion between 4.8–5.2 MeV.

TABLE I. Concentration of accelerated ions for a heated and unheated aluminum target.

	Protons	C ⁵⁺	C ⁴⁺	C ³⁺	C ²⁺	C ¹⁺
Unheated	1E12	2.2E9	2.3E10	2.4E10	1.8E10	1.3E10
Heated	~8E10	4.5E9	1E11	5.7E10	3.3E10	2E10

There is a slight indication of another line between those labeled A and B, but its proximity to the line at 5 MeV makes it difficult to distinguish from the background noise of the film.

Using nuclear emulsions behind the DEF allowed cross calibration for exact proton counting. Integrating the area under the spectrum shown in Fig. 6 above 5 MeV where calibration is exactly known, gives a proton yield of 1.77×10^{11} . Fitting the curve to a single exponential decay [$N(E) \propto e^{-E/E_0}$] gives the temperature of the spectrum to be $E_0 = 4.7$ MeV. Using this, we can calculate the average energy per proton, $\langle E \rangle = 7.7$ MeV, which translates into 218 mJ of energy or 1.0% of laser energy for this shot converted into kinetic energy of protons.

IV. THEORETICAL MODEL AND DISCUSSION

Here we present a 2D particle-in-cell (PIC) simulation that incorporates multiple ion species for short-pulse, high-intensity laser–plasma interactions. The target is a thin Au foil of thickness $7 \mu\text{m}$. The target ions are almost immobile, on the time scales of the simulation, due to their large mass. In front of the foil, is a preformed-plasma with scale length near critical density of approximately $3 \mu\text{m}$. This differs slightly from the actual experiment where a preplasma of scale length $\sim 30 \mu\text{m}$ existed up to $100 \mu\text{m}$ in front of the target. On the back surface of the target, we put a 100 \AA CH layer. The target is fully ionized initially and the population of carbon charge states is set to $C^{4+}:C^{3+}:C^{2+}:C^{1+} = 5:3:2:1$ based on the experimental results.¹³

The laser pulse is at normal incidence to the target with a peak intensity of $2 \times 10^{19} \text{ W/cm}^2$. The laser pulse was specified as p -polarized which is significant in a 2D simulation since the local angle of incidence is subject to change as the plasma surface is deformed. The total pulse duration is about 300 fs with a Gaussian profile. The transverse profile is also Gaussian and its $1/e^2$ spot size is set to $5 \mu\text{m}$. The simulation time continued for an additional 150 fs after the pulse was switched off to observe the final proton energy.

Figure 7 shows the 2D PIC simulation results. The simulation parameters are not exactly those of the experiment due to computational limitations. However, they are close enough to see the detail of proton acceleration in multispecies expansion in the present energy range. The plot of Fig. 7(a) shows the ions $X-V_x$ phase-space plots after laser irradiation. All species of the carbon ion charge states are completely separated in space at this final stage, and the electrostatic field has distinguishable peaks at the ion expansion fronts as discussed in Ref. 17. The final energy of the C^{4+} ions is reduced to approximately one-half of the expected energy from the charge-mass ratio, due to the presence of protons at the expansion front. Similarly, the acceleration of the lower carbon charge states is reduced by the presence of the higher charge state species.

The proton energy spectrum at the end of the simulation (450 fs) is shown in Fig. 7(b). The low energy cutoff in the spectrum arises because the protons are completely detached from the target surface. It is an interesting artifact of the simulation, but is not meant to show agreement with the

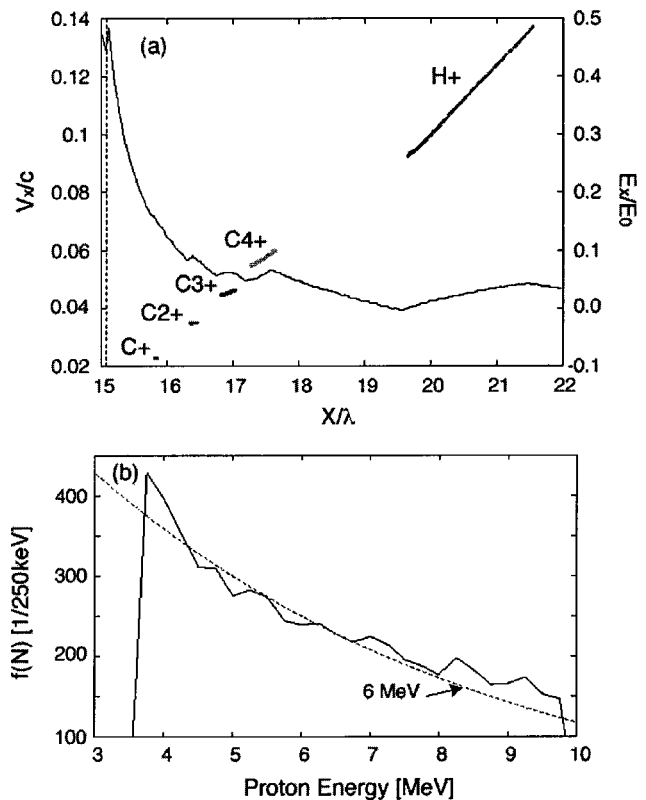


FIG. 7. 2D-PIC simulation results. (a) Phase plots $X-V_x$ of ions and longitudinal profile of the electrostatic field observed at 370 fs. The broken line indicates the initial CH layer surface. (b) The proton energy spectrum at 450 fs.

low energy cutoff in the presented data. As mentioned above, the magnetic spectrometer had a lower detection threshold of 3 MeV.

Although the slope of the spectrum in the simulation (6 MeV) is slightly higher than the experimental result (4.7 MeV), the spectrum in the simulation has similar modulations to those of the experimental result shown in Fig. 6. It has been shown computationally, that a proton spectrum can exhibit a monoenergetic peak at the deuteron-ion front in an overlapped multispecies expansion from a thick target.¹⁷ In the present case, however, the protons are completely separated from the other ion species. Although these modulations in the simulated spectrum are small, they are not the result of numerical noise. The observed modulations are attributed to multispecies effects described below.

The maximum proton energy in the simulation (10 MeV) is smaller than that of the experiment (12 MeV). It is known that the maximum ion energy depends on the hot electron temperature, namely, the laser intensity⁹ but it also depends on the target thickness and the preplasma scale length¹⁸ both of which are smaller in the simulation than in the experiment. It is also possible that the protons have not reached their maximum energy in the 350 fs for which the simulation is run.

To see the details of acceleration process, we performed a 1D PIC simulation using the same parameters, with a slightly higher laser intensity of $5 \times 10^{19} \text{ W/cm}^2$. Two types of thin layers were simulated, the first consisting of purely

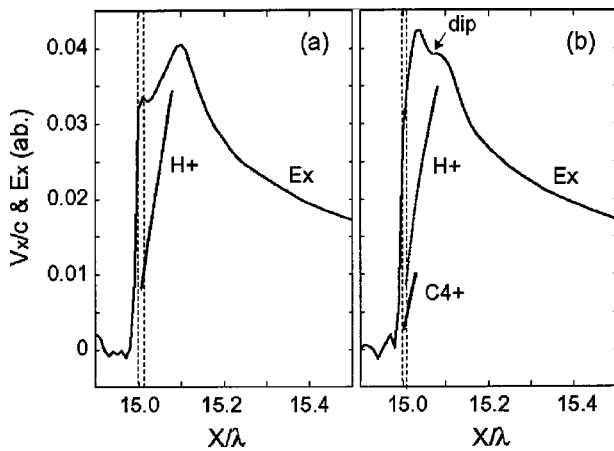


FIG. 8. (1D-PIC) The longitudinal electrostatic field profile with the ion phase plots at $t=105$ fs in the case of (a) pure proton layer and (b) CH mixture. The broken lines indicate the initial thin layer location. The electrostatic fields are cycle averaged in a one laser oscillation period to remove the high frequency component (high frequency component does not affect the ions).

protons and the other of a C–H mixture. Figure 8 shows the longitudinal profile of the electrostatic field and the ions phase plot early in time, at the start of the acceleration process. In the case of the pure proton layer [Fig. 8(a)], the electrostatic field, E_x , has one strong peak at the proton expansion front. Therefore, the protons at the front are always accelerated more than those directly behind the front. So the spectrum exhibits no bunching. They are simply expanding both in real-space and energy-space. Alternatively, in the case of the CH mixture, a peak in E_x appears in the middle of the proton distribution due to the presence of the carbon ions. In this case, the protons near the peak in E_x are accelerated more than those near the dip of E_x [Fig. 8(b)]. From this, we infer that the presence of the peak in E_x near the middle of the expansion is responsible for the observed bunching in the spectrum.

Figure 9 shows the time evolution of the proton energy spectrum from the CH layer. Modulations in the proton spectrum are visible at $t=130$ fs, approximately eight laser periods later in time from the spectra shown in Fig. 8. After the protons move ahead of the carbon ion fronts, they are accelerated continuously to higher energies and then drift in space after leaving the region of the electrostatic field. The later-

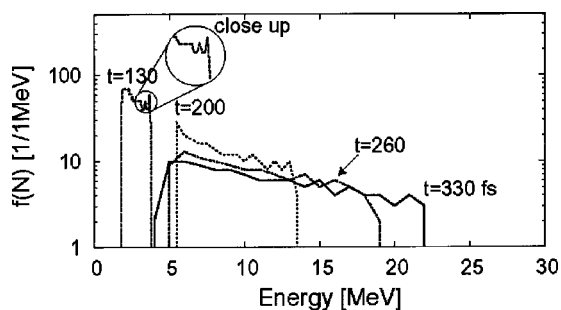


FIG. 9. (1D-PIC) The time evolution of the proton energy spectrum in the case of a CH layer ($0.01 \mu\text{m}$).

time spectra shown in Fig. 3, demonstrate the structure imprinted on the protons initially, remains as the protons thermally expand during propagation.

Here, we simply estimate the expected position of bunching in the spectrum. Imprint occurs very early in time during the acceleration. At that time, the ion acceleration simply depends on the particle's charge-mass ratio, of H^+ to C^{4+} . The accumulation of protons occurs at the dip of the electrostatic field, which appears around the middle of the expansion fronts of H^+ and C^{4+} , cf. Fig. 8(b). Assuming the protons and carbon ions are accelerated in the identical field, we can find the velocity of the bunching position,

$$\frac{V_{P\text{bunch}}}{V_{P\text{max}}} = \sqrt{\left(1 + \frac{q_c M}{e M_c}\right)} / 2, \quad (2)$$

where $V_{P\text{bunch}}$ and $V_{P\text{max}}$ are the proton velocity of the bunch and the maximum respectively, and e, M (q_c, M_c) are the proton's (carbon's) charge and mass. Therefore the energy of the bunch is expected as

$$\frac{E_{P\text{bunch}}}{E_{P\text{max}}} = \left(1 + \frac{q_c M}{e M_c}\right) / 2. \quad (3)$$

Under the current parameters using the charge and mass of C^{4+} , the bunch's energy is expected to be approximately 65% of the maximum proton energy. This agrees well with the simulation results. The strong line, labeled A, in the experimental data of Fig. 6 appears at 9 MeV, which is close to the 8.5 MeV predicted by Eq. (3). It may be possible that a small amount of higher charge state carbons, C^{5+} , contribute to pushing the bunch to a slightly higher energy.

V. CONCLUSION

We have shown that the maximum energy of protons appears to be correlated with laser-irradiation scaling as $E_{\text{max}} \propto (\lambda^2)^{0.5}$ and decreases at angles greater than normal incidence. Total number of protons with energy above 5 MeV is $> 10^{11}$ protons per shot, which is at least a 1% conversion efficiency of the laser energy.

We have also shown experimental evidence of visible modulations in proton spectra. Lines around the 9 MeV ($\pm 1-2$ MeV) range appear on the film in approximately 30% of the shots. We believe them to be caused by the presence of multiple ion species. Carbon ions, present on the target in the form of contaminants, can enhance the accelerating electric field in the region of the carbon ion front. This effect on the electric field may be evident in the form of visible lines that appear in proton spectra at a percentage of the maximum proton energy. The experimental observations agree well with PIC models that show the structure imprinted on the protons initially, remains as the protons thermally expand during propagation.

Clearly understanding the effect heavy ions have on proton acceleration will enhance our understanding of the acceleration mechanism. The possibility exists for shaping the proton spectrum by doping targets with various concentrations of heavy ions. If the proton spectrum could be efficiently shaped at specific energies instead of a continuum

energy spread, applications such as medical isotope production and proton injector schemes for conventional particle accelerators could become more feasible.

ACKNOWLEDGMENTS

We gratefully acknowledge the LULI-laser team for their kind support. LULI is UMR 7605, NRS-CEA-Université Paris VI/Ecole Polytechnique.

This work was also supported primarily by the EU Program No. HPRI CT 1999-0052 and in part by Grant No. E 1127 from Région Ile-de-France, and by corporate support from General Atomics. This work was performed under the auspices of the U.S. Department of Energy by the University of California, Lawrence Livermore National Laboratory under Contract No. W-7405-Eng-48.

¹F. Begay and D. Forslund, *Phys. Fluids* **25**, 1675 (1982).

²S. J. Gitomer, R. Jones, F. Begay, A. Ehler, J. Kaphart, and R. Kristal, *Phys. Fluids* **29**, 2679 (1986).

³M. D. Perry and G. Mourou, *Science* **264**, 917 (1994).

⁴A. Maksimchuk, S. Gu, K. Flippo, D. Umstadter, and V. Bychenkov, *Phys. Rev. Lett.* **84**, 4108 (2000).

⁵E. Clark, K. Krushelnick, J. Davies *et al.*, *Phys. Rev. Lett.* **84**, 670 (2000).

⁶A. Puhkov, *Phys. Rev. Lett.* **86**, 3562 (2001).

⁷S. C. Wilks and W. L. Kruer, *IEEE J. Quantum Electron.* **33**, 1954 (1997).

⁸S. P. Hatchett, C. G. Brown, T. E. Cowan *et al.*, *Phys. Plasmas* **7**, 2076 (2000).

⁹S. C. Wilks, A. B. Langdon, T. E. Cowan, M. Roth, M. Singh, S. Hatchett, M. H. Key, D. Pennington, A. MacKinnon, and R. A. Snavely, *Phys. Plasmas* **8**, 542 (2001).

¹⁰A. J. Mackinnon, M. Borghesi, S. Hatchett, M. H. Key, P. K. Patel, H. Campbell, A. Schiavi, R. Snavely, S. C. Wilks, and O. Willi, *Phys. Rev. Lett.* **86**, 1769 (2001).

¹¹R. Snavely, M. H. Key, S. P. Hatchett, T. E. Cowan, M. Roth, T. W. Phillips, M. A. Stoyer, E. A. Henry, T. C. Sangster, and M. S. Singh, *Phys. Rev. Lett.* **85**, 2945 (2000).

¹²T. E. Cowan, M. Roth, J. Johnson *et al.*, *Nucl. Instrum. Methods Phys. Res. A* **455**, 130 (2000).

¹³M. Hegelich, S. Karsch, G. Pretzler, D. Habs, K. Witte, W. Guenther, M. Allen, A. Blazevic, J. Fuchs, J. C. Gauthier, M. Geissel, P. Audebert, T. Cowan, and M. Roth, *Phys. Rev. Lett.* **89**, 085002 (2002).

¹⁴P. A. Jansson, *Deconvolution of Images and Spectra* (Academic, New York, 1997).

¹⁵E. L. Clark, K. Krushelnick, M. Zepf *et al.*, *Phys. Rev. Lett.* **85**, 1654 (2000); F. N. Beg, A. R. Bell, A. E. Dangor *et al.*, *Phys. Plasmas* **4**, 447 (1997).

¹⁶P. D. Rockett, C. R. Bird, C. J. Hailey, D. B. Brown, and P. G. Burkhalter, *Appl. Opt.* **24**, 2536 (1985).

¹⁷Y. Murakami, Y. Kitagawa, Y. Sentoku, M. Mori, R. Kodama, K. A. Tanaka, K. Mima, and T. Yamanaka, *Phys. Plasmas* **8**, 4138 (2001).

¹⁸Y. Sentoku, V. Y. Bychenkov, K. Flippo, A. Maksimchuk, K. Mima, G. Mourou, Z. M. Sheng, and D. Umstadter, *Appl. Phys. B: Lasers Opt.* **B74**, 207 (2002).